

# Three-dimensional microscale numerical simulation of smoldering

G. Debenest<sup>(1)</sup>, V.V. Mourzenko<sup>(2)</sup>, J.-F. Thovert<sup>(2)</sup>

<sup>(1)</sup> Institut de mécanique des fluides de Toulouse UMR CNRS/INPT UPS 31400 Toulouse.

<sup>(2)</sup> Laboratoire de Combustion et de Détonique, CNRS, Chasseneuil du Poitou, France

## Abstract

A three-dimensional numerical tool for the simulation of smoldering in fixed beds of solid fuels is presented in this paper. The description is based on the microscale equations, in a detailed discretized image of the porous medium. Simplifying assumptions are used, but the local coupling of the transport and reaction mechanisms is fully preserved. A set of 2D and 3D simulations demonstrates the ability of the model to handle a variety of situations, and to provide detailed local information. In particular, it is shown that severe thermal disequilibrium exists in some regimes, which preclude a straightforward application of simple macroscopic models.

*Key words:* Smoldering, Microscale Simulation, Oil shale, Porous media

## Introduction

We address here the numerical simulation of smoldering in fixed beds of solid fuels. A very general simulation tool was built, with two main purposes in mind. First, it may be used for direct simulations in actual situations, and for parametric studies that may be easier to carry out numerically than experimentally. Second, on a more fundamental level, it may be used to assess how far homogenized macroscopic descriptions are applicable, and to provide estimates for the effective coefficients that would then be involved.

A macroscopic point of view is adopted in most theoretical studies, whereby the medium is regarded as a continuum (see *e.g.*, [1,2]). The equations involve effective parameters such as dispersion coefficients or mean volumetric reaction rates, and they relate macroscopic fields that represent volume averaged local quantities. However, the effective coefficients depend on the medium microstructure and on the flow and reaction regimes, and their determination generally requires the solution of the full set of microscale equations in a representative sample [3]. In addition, the validity of homogenized equations is also questionable, in view of the strong gradients on the microscopic scale. Finally, local non-equilibrium plays an important role in many respects, such as in pollutant formation, and

it can only be modeled by detailed local simulations [4].

For these reasons, we developed a simulation tool based on a microscopic description, where the local equations are solved in a detailed discretized image of the microstructure. We are not aware of any prior attempt fully along these lines. A fully detailed statement of the problem at the microscopic scale is provided in the review paper [5]. In view of the complexity of the problem, which stems mostly from the complexity of the domain geometry and from the non linearity of the equations, various simplifications are used here, but the main feature that we want to investigate is preserved, which is the coupling at the microscale of the transport and reaction processes.

## Physical and mathematical models

In order to remain anchored to reality, the materials and operating parameters corresponding to a lab-scale experiment [6] are used as reference case. Ground Moroccan oil shale, with a typical grain size  $\Phi=600\ \mu\text{m}$ , is packed in a vertical column. Inert sand grains can be added in various proportions. Air is blown from the bottom, where ignition is performed. A reaction front propagates upwards, where the temperature may rise up to about 1000–1200K. Pyrolytic reactions occur downstream of the front; the kerogen decomposes into gaseous compounds that are taken away by

the flow and a solid carbon char that later reacts with the oxygen. The flow rate can be varied. The Reynolds number  $Re$  does not exceed 2.7, and the Péclet number  $Pe$  (see Eq. 9) ranges from 1 to 10.

For lack of chemical data, the pyrolytic processes are not considered, although they could be easily introduced in the model. Thus, the chemical processes reduce to the exothermal oxidation of the carbon char. Since the fraction of kerogen in the shale is moderate, the geometry of the bed is unchanged during the process.

Hence, the mathematical model only involves governing equations for the gas flow, for the oxygen and heat transports, a balance equation for the carbon char and a kinetic model for the surface chemical reaction. However, the problem is still very complex, and additional approximations of various natures are used, which are detailed below.

Gas flow. Since  $Re$  is at most of the order of unity, inertial effects are ignored and the flow in the pore space  $\Omega_g$  is described by the Stokes equations

$$\nabla p = \mu \nabla^2 \mathbf{v} , \quad \nabla \cdot \mathbf{v} = 0 \text{ in } \Omega_g \quad (1)$$

where  $p$  is the pressure and  $\mathbf{v}$  is the velocity. A no-slip condition  $\mathbf{v} = 0$  is applied on the pore surface  $\partial\Omega$ .

Variations of the density  $\rho$ , of the dynamic viscosity  $\mu$  and of the other physicochemical

coefficients in the following equations with the gas temperature and composition are not taken into account.

Transport of the oxidizer. The oxygen is conveyed by the gas, and its concentration  $c_o$  is governed by a convection-diffusion equation

$$\partial c_o / \partial t + \nabla \cdot (\mathbf{v} c_o - D_o \nabla c_o) = 0 \quad \text{in } \Omega_g \quad (2)$$

where  $D_o$  is the diffusion coefficient.

Carbon char balance. This balance equation only involves the decay due to the chemical reaction. Only a global balance is kept, on a per grain basis.

Heat transport. Two heat transport equations are written, in the gas phase  $\Omega_g$  and in the solid phase  $\Omega_s$ . The former is a convection-diffusion equation, whereas the latter only involves conduction

$$C_g \partial T / \partial t + \nabla \cdot (C_g \mathbf{v} T - \lambda_g \nabla T) = 0 \quad \text{in } \Omega_g \quad (3a)$$

$$C_s \partial T / \partial t - \lambda_s \nabla^2 T = 0 \quad \text{in } \Omega_s \quad (3b)$$

where  $C_i$  is the volumetric heat capacity of phase  $i$ , and  $\lambda_i$  its heat conductivity.

These transport equations are coupled by the continuity of the temperature across  $\partial\Omega$ , and by the source and sink terms associated with the surface reaction (see Eq. 6). The system is completed by macroscopic upstream boundary

conditions, *i.e.*, by the gas flow rate, the entry gas temperature and oxygen concentration.

**Chemical model.** The oxidation of the carbon char takes place within the shale grains, where the char resides, and multiple reaction steps are certainly involved. However, from the point of view of the present pore-scale description, each grain behaves as a "micro-reactor", described by a global black-box approach, reminiscent of the "one-film model" of [7]. The whole reaction scheme is summarized by a global exothermal heterogeneous reaction, that takes place on the surface  $\partial\Omega$  of the shale grains,



The reaction kinetic is supposed to be of first order with respect to  $O_2$ , with a rate coefficient given by Arrhenius law. However, the activation energy is supposed to be large enough, so that a sharp transition exists between a low-temperature kinetically controlled regime, where the reaction rate is very small, and a high-temperature diffusionnally controlled regime. Thus, the kinetic law finally reduces to the bimodal model

$$\left\{ \begin{array}{l} \text{Negligible reaction if } T < T_r \\ \text{Diffusion limited if } T > T_r \end{array} \right. \quad (5)$$

The reaction induces source and sink terms  $S_O$ ,  $S_T$  and  $S_C$  for the oxygen, the heat and the carbon, that are all proportional to the reaction rate. The source  $S_T$  and the sink  $S_O$ , localized on the surface

$\partial\Omega$  of the reactive grains, yield the following boundary conditions

$$-D_O \mathbf{n} \cdot \nabla c_O + S_O = 0 \quad \text{on } \partial\Omega \quad (6a)$$

$$\mathbf{n} \cdot (\lambda_s \nabla_s T - \lambda_g \nabla_g T) + S_T = 0 \quad \text{on } \partial\Omega \quad (6b)$$

where  $\mathbf{n}$  is the unit normal vector to  $\partial\Omega$ .

### Numerical model

The numerical code is described in details in [8]. Only its main features are recalled here.

**Geometrical model.** The bed geometry is described by a 3D array of gaseous or solid cubes. Since the microscale is much smaller than the whole domain size, the medium is regarded as transversally unbounded, with a spatially periodic solid phase distribution. Realistic samples of randomly deposited grain packings are built by use of the tools described in [9]. An example is shown in Fig. 1. Two-dimensional simulations can also be conducted, for a faster preliminary sweep of the parameters and an easier graphical display of the results.

**Flow solution.** Owing to the approximations made in the formulation of the flow problem, the velocity field is unaffected by the temperature field and since the geometry of the solid phase is spatially periodic, the velocity field is periodic as well. The flow solver [9,10] makes use of an artificial compressibility method, with a finite

difference scheme on a staggered marker-and-cell mesh.

Transports in the gas phase. Both oxygen and heat transport by the flowing gas are described by random walk algorithms, that account for the convection and diffusion mechanisms [11,12]. The transported quantity is represented by Brownian particles, whose trajectories are constructed by small time steps, during which they undergo a deterministic displacement according to the local conveying fluid velocity and a random diffusive displacement.

The time step  $\delta t$  is set so that the elementary displacements never exceed half the grid step size. The amounts  $q_o$  and  $q_T$  of oxygen and heat represented by the elementary particles result from a compromise between computational cost and statistical stability.

Heat conduction in the solid. The application of the same method to describe heat conduction in the solid phase requires a prohibitive number of thermal particles, due to the much larger volumetric heat capacity. Hence, we use instead a finite difference scheme. Original techniques were devised for the matching of the random walk and finite difference descriptions at the gas/solid interface.

Surface reaction. Any time an oxygen particle hits the surface of a shale surface element, on a grain that still contains carbon, the reaction (4) is

implemented if the local temperature exceeds the threshold value  $T_r$ . The oxygen particle is removed from the system, the carbon content of the grain is decremented by the stoichiometric amount, and thermal particles are released on  $\partial\Omega$  that will afterwards spread in the gaseous and solid phases.

If so desired, the reaction products can also be tracked. For instance, new particles representing  $\text{CO}_2$  can be followed until they exit the system. It is also possible to take into account other species, such as  $\text{CO}_x$  or  $\text{NO}_x$ , according to the local conditions. The possibility of such an extension is one of the main interests of the microscopic approach.

Parameters of the simulation. The system is characterized by a set of geometrical parameters (bed geometry, volume fractions, porosity  $\epsilon$ ), and by the physical properties of the constituents. Their values, estimated at 1000K, which is a typical temperature in the region of the reaction zone, are listed in Table 1.

The chemical model requires the knowledge of the volumetric amount of carbon, the corresponding heat release and the threshold temperature  $T_r$ . The first one was estimated from the experimental data. The heat release  $q$  in (4) is taken equal to the enthalpy of formation 395 kJ/mol of  $\text{CO}_2$  at 1000K. Finally, measurements on oil shales similar to ours [13] showed that the

reaction (4) is initiated at about 500K and that the carbon is exhausted at about 750K. Thus,  $T_r$  can be safely set in this range.

Three important parameters can be derived from these data. The adiabatic temperature  $T_{ad}$  results from the ratio of the volumetric heat production and heat capacity; the ratio  $U_F/v;^-$  of the front velocity to the gas seepage velocity results from the stoichiometry and from the carbon content. In the experiment, it is equal to  $3.4 \cdot 10^{-3}$  for a mixture of shale and sand in equal volume; finally, the parameter  $\Delta$ , related to the net heat flux through the front, which greatly determines the global behavior of the system,

$$\Delta = \frac{\varepsilon C_g (v^* - U_F)}{[\varepsilon C_g + (1 - \varepsilon) C_s] U_F} \approx \frac{\varepsilon C_g}{(1 - \varepsilon) C_s} \frac{v^*}{U_F} \quad (7)$$

It can be shown by a simple 1D continuous model [14] that if  $\Delta > 1$  (large fuel or low oxidizer concentrations), heat is transferred from the upstream to the downstream region. An asymptotic temperature profile with a plateau  $T_p$  on the downstream side is expected. In the opposite case  $\Delta < 1$ , the plateau is expected on the upstream side. The intermediate case  $\Delta = 1$  corresponds to the ultimate superadiabatic situation, where heat remains in the vicinity of the reaction front. The experimental conditions correspond to  $\Delta = 0.1 \sim 0.34$ , depending on the amount of inert sand. Note that  $\Delta$  can also be

expressed as a function of the heat capacities and of the volumetric concentrations of carbon ( $c_c$ , in the solid) and oxidizer ( $c_o$ , in the gas) [14],

$$\Delta \approx (C_g/C_s)(c_c/c_o) \quad (8)$$

Finally the gas flow rate has to be specified. It is quantified by the dimensionless Péclet number

$$Pe = v^* L / D_o \quad (9)$$

where  $v^* = v;^- / \varepsilon$  is the mean interstitial velocity and  $L$  is a characteristic length of the microstructure.  $Pe$  is the ratio of the diffusion time  $L^2/D_o$  to the convective time  $L/v^*$ ; hence, it is expected to control the transfer rate of oxygen toward the reactive walls.

The dimensionless parameters  $\Delta$  and  $Pe$  (or the related quantity  $Pe_{Fs}$  in Eq. 10) fully determine the global behavior of the system, regardless for instance of the grain size  $\Phi$ .

## Results

### *Two-dimensional simulations.*

A set of 2D results has been presented in [14], which focused on the typology of the regimes according to the range of the governing dimensionless parameters. We considered the simple model of a staggered array of cylinders (Fig. 2), with diameter  $\Phi$ . The porosity is  $\varepsilon = 0.356$ . The length scale  $L$  is the longitudinal period  $6\Phi/5$ . It was confirmed that  $\Delta < 1$  and  $\Delta > 1$  correspond to reaction-leading and reaction-

trailing situations, respectively. In addition, it was shown that local thermal equilibrium is fulfilled or not, according to the value (lower or larger than unity) of a Péclet number

$$Pe_{Fs} = C_s U_F L / \lambda_s \quad (10)$$

This parameter compares the characteristic times for the reaction front advancement and for heat redistribution in the solid. These observations are illustrated in Fig.2.

### *Three-dimensional simulations.*

We focus now on a realistic simulation of the reference experimental setup. We operate in the random grain packing depicted in Fig. 1. The bed porosity is  $\varepsilon=0.406$  and  $L=8\Phi$ . Various situations have been investigated, which roughly correspond to the range covered in the experiments (see Table 2).

The Péclet number  $Pe$  was taken equal to 2 or 10, and the bed was composed of a fraction  $p_s$  of reactive shale grains and  $1-p_s$  of inert sand grains, with  $p_s=1$  or  $1/2$ . The carbon content in the shale was set to  $c_c=9190 \text{ mol/m}^3$ , which roughly corresponds to the actual value, or to  $c_c=5195 \text{ mol/m}^3$ . Both  $p_s$  and  $c_c$  affect the parameter  $\Delta$ , which in turn is independent of the gas flow rate.

The simulations are conducted in two steps. The first one corresponds to the ignition. Since the bed is initially at room temperature  $T_0$ , we

first run for a while without taking the criterion (5) into account, until a sufficient temperature has developed for the process to sustain itself. After the reaction front has reached a position  $X_F = 8\Phi$ , we introduce the oxidation kinetic law represented by (5).

First stage: Ignition: During this initial period, the chemical model is very rough but nonetheless, the system evolves according to the expected trends. This stems from the fact that temperature often exceeds  $T_r$  in a region which covers and exceeds the actual reaction zone, as can be checked *a posteriori* when Eq. (5) is used, and therefore applying or not this criterion makes little difference.

Examples of temperature and oxidizer concentration fields are shown in Fig. 3, at successive instants. Colors range from  $T_0$  (dark blue) to  $1.2 T_{ad}$  (dark red) for  $T$ , and from 100% (blue) to 0% (red) of the entry oxygen concentration. Clearly, a progressive thermal layer develops, with increasing length and temperature;  $T$  exceeds  $T_{ad}$  in the latest stage. Conversely, the reaction layer remains of a fairly constant thickness, as shown by the oxidizer concentration which drops to 0 over a few grain sizes.

Figure 4 and 5 compare the situations reached when  $X_F = 8\Phi$ , for the two values of the carbon

content  $c_c$ , and for two values of the flow rate and of the bed composition in each case. The heterogeneity of the temperature field is clearly correlated with the value of  $Pe_{Fs}$ . Thermal non-equilibrium can exist between the grains and the surrounding gas (e.g., bottom-right frame in Fig. 5), or over a larger range, in cases when reactive shales grains are mixed with inert sand (top-right frames in Figs. 4 and 5).

Examples of transversally averaged temperature profiles are shown in Fig. 6, in the four cases with  $Pe_{\sigma}=2$ , and at three successive instants. Although a steady regime is not reached yet, the build-up of an upstream temperature plateau is perceptible. Recall that the plateau should settle at  $T_p=T_{ad}/|1-\Delta|$  [14]. As theoretically predicted, the closer  $\Delta$  is to unity, the slowest is the transient to the asymptotic regime.

Second stage: Kinetics described by Eq. (5):  
 The simulations were carried on starting from the states reached for  $X_F=8\Phi$ , by applying the criterion (5) with a threshold  $T_r=T_0+300^\circ$ . In addition, a probability  $\Pi_r$  of reaction was introduced, which supplements (5) for determining whether a reaction occurs whenever an oxidizer "particle" hits a wall. This quantity, which is equal here to  $\Pi_r=0.02$ , accounts in a first approximation for the fact that the char sits within the shale grains, which the oxidizer has to penetrate. It describes the probability for the

particle to enter the grain and find a reactive site, and it results from an estimate of the diffusive exchanges between the inter- and intra-granular porosities [15]. The case of a real surface reaction, with  $\Pi_r=1$ , was also considered.

Mean temperature and oxidizer concentration profiles are shown at regularly spaced successive instants in Figs. 7 and 8, for  $\Pi_r=1$  and 0.02, respectively. As already mentioned, the introduction of the kinetic law makes little difference when  $p_s=\Pi_r=1$ ; the build-up of the upstream plateau proceeds smoothly, there is no oxidizer left in the outgoing gas, and the front velocity  $U_F$  is unchanged. When  $\Pi_r=0.02$ , about 10% of the oxidizer crosses the reaction zone without reacting, and the front progression slows down accordingly.

These effects are amplified when  $\Pi_r=0.02$ ; about 20% (for  $p_s=1$ ) or even 50% (for  $p_s=1/2$ ) of the oxidizer escapes on the downstream side. It seems for a while that the temperature is going to stop growing, and even to decrease, which could possibly cause extinction, but the significant reduction of  $U_F$  concentrates the reduced heat production in a narrower region and eventually, the build-up of the upstream plateau resumes.

One of the most interesting features of the simulation tool, for future developments, is the detailed account of the processes on the

microscale, which gives access to the local thermochemical conditions under which the reactions take place. An example is provided in Fig. 9. The distribution of the temperature and oxidizer concentration at the location of each elementary reaction is shown when the reaction front has reached  $X_f=15\Phi$ . The situation corresponds to a late stage in the top row of Fig. 7.

Another example is given in Fig. 10. The surfaces which bound the region hotter than  $T_r=300^\circ\text{C}$ ,  $T_{ad}=1076^\circ\text{C}$ ,  $T_p=1630^\circ\text{C}$  and  $2000^\circ\text{C}$  are shown in the same situation as in Fig. 9. The region where  $T > T_r$  widely exceeds the reaction zone. The temperature is also higher than  $T_{ad}$  in a wide region, and it has reached  $T_p$  in a layer about  $4\Phi$  thick. Significantly larger temperatures are observed in a few hot spots.

### Conclusion and perspectives

These applications demonstrate the ability of the numerical tool to handle a variety of situations, to reproduce and predict global behaviors and to yield detailed local thermochemical information. It provides an avenue for a sensible macroscale modelling of smoldering processes. It also constitutes a starting point for several highly interesting extensions. Some of them are underway, associated with the implementation of a more elaborate chemical model, while taking advantage of the knowledge

of the local thermochemical conditions. This includes the emission of noxious species such as carbon monoxide. Pyrolytic processes could also be accounted for, as well as the possible reaction of the volatile species with the oxidizer.

### Acknowledgements

Most computations were performed at CINES (Montpellier, France), subsidized by the MENESR, whose support is gratefully acknowledged.

### References

1. Moallemi, M.K., Zhang, H. and Kumer, S., *Combust. Flame*, 95 (1993) 170-182.
2. Aldushin, A.P., Rumanov, I.E. and Matkwosky, B.J., *Combust. Flame* 50 (1999) 76-90.
3. Adler P.M., and Thovert J.F, *Appl. Mech. Rev.*, 51 (1988) 537-585.
4. Oliveira, A.A.M. and Kaviany, M., *Prog. Ener. Combust. Sci.*, 27 (2001) 523-545.
5. Ohlemiller, T.J., *Prog. Ener. Combust. Sci.*, 11 (1985) 277-310.
6. Ahd, M., Bruel, P., Deshaies, B., and Vantelon, J.-P., unpublished.
7. Turns, S.R., *An introduction to combustion; Concepts and applications*, McGraw-Hill, New-York, 1996.
8. Debenest G., V.V. Mourzenko, J.-F. Thovert, *Combust. Theory Modelling*, 9 (2005) 113-135.

9. Coelho, D., Thovert J.-F. and Adler, P.M., *Phys. Rev. E*, 55 (1997) 1959-1978.
10. Lemaître, R. and Adler, P.M., *Transp. Porous Media*, 5 (1990) 325-340.
11. Sallès, J., Thovert, J.-F. and Adler, P.M., *Chem. Eng. Sci.*, 48 (1993) 2839-2858.
12. Békri, S., Thovert, J.-F. and Adler, P.M., *Chem. Eng. Sci.*, 50 (1995) 2765-2791.
13. Nabih, K., Boukhari, A., Real, M. and Arnada, M.A.G., *Ann. Chim. Sci. Mat.*, 50 (1998) 389-393.
14. Debenest G., V.V. Mourzenko, J.-F. Thovert, *Combust. Theory Modelling*, 9 (2005) 301-321.
15. Debenest G., Ph.D. Thesis, Univ. de Poitiers, 2003.

**TABLES:**

**Table 1.**

Physical constants for the constituents, at T=1000K.

	Gas	Solid (shale or sand)
$\rho$ [kg m <sup>-3</sup> ]	0.348	2700
$C$ [J K <sup>-1</sup> m <sup>-3</sup> ]	397	3.375 10 <sup>6</sup>
$D_0$ [m <sup>2</sup> s <sup>-1</sup> ]	2 10 <sup>-4</sup>	-
$\lambda$ [W K <sup>-1</sup> m <sup>-1</sup> ]	0.07	1

**Table 2.**

Parameters for the grain packing, at T=1000K.

	$Pe$	$\Delta$	$Pe_{Fs}$	$T_{ad}$
$c_c = 5195$ mol/m <sup>3</sup>	2	0.19	0.5	608
$p_s = 100\%$ shale	10	0.19	2.57	
$c_c = 5195$ mol/m <sup>3</sup>	2	0.095	1	304
$p_s = 50\%$ shale	10	0.095	5.15	
$c_c = 9190$ mol/m <sup>3</sup>	2	0.34	0.29	1076
$p_s = 100\%$ shale	10	0.34	1.45	
$c_c = 9190$ mol/m <sup>3</sup>	2	0.17	0.57	588
$p_s = 50\%$ shale	10	0.17	2.9	

## Figure captions

**Figure 1.** Example of a numerically deposited grain packing. Colors in the pore space corresponds to the magnitude of the gas velocity.

**Figure 2:** Temperature field during a smoldering process in a 2D array of cylinders in various regimes.

**Figure 3:** Ignition stage in a 3D bed of spheres. The temperature field is shown on the left for three successive positions  $X_f$  of the reaction. The corresponding oxygen concentration fields are shown on the right. Data are for  $Pe = 10$ ,  $p_s = 1/2$ ,  $c_c = 9190 \text{ mol/m}^3$ ,  $\Delta = 0.34$  and  $Pe_{Fs} = 1.45$ .

**Figure 4:** The temperature fields in four situations when  $X_f = 8\Phi$ , for  $c_c = 9190 \text{ mol/m}^3$ . The same scale is used in the all cases. .

**Figure 5:** The temperature fields in four situations when  $X_f = 8\Phi$ , for  $c_c = 5195 \text{ mol/m}^3$ . The same scale is used in the all cases. .

**Figure 6:** Transversally averaged temperature profiles in the four situations in Figs. 4,5 with  $Pe = 2$ , when  $X_f = 2\Phi$ ,  $5\Phi$  and  $8\Phi$ . The dashed line shows the adiabatic temperature  $T_{ad}$  in each situation.

**Figure 7:** Mean profiles of T (left) and  $c_o$  normalized by the entry gas concentration (right), at successive and regularly spaced instants. Data are for  $Pe = 10$ ,  $p_s = 1$ ,  $c_c = 9190 \text{ mol/m}^3$ ,  $T_r = T_0 + 300^\circ$  and  $I_r = 1$ .

**Figure 8:** Mean profiles of T (left) and  $c_o$  normalized by the entry gas concentration (right), at successive and regularly spaced instants. Data are for  $Pe = 10$ ,  $p_s = 1$ ,  $c_c = 9190 \text{ mol/m}^3$ ,  $T_r = T_0 + 300^\circ$  and  $I_r = 0.02$ .

**Figure 9:** Thermochemical conditions at the reaction sites. Data are for  $Pe = 10$ ,  $p_s = 1$ ,  $c_c = 9190 \text{ mol/m}^3$ ,  $T_r = T_0 + 300^\circ$  and  $X_f = 15\Phi$ .

**Figure 10:** Boundaries of the regions where  $T$  exceeds  $T_r = 300^\circ\text{C}$  (blue),  $T_{ad} = 1076^\circ\text{C}$  (cyan),  $T_p = 1630^\circ\text{C}$  (yellow) and  $2000^\circ\text{C}$  (red). The axes are graduated in grain sizes  $\Phi$ . Data are for  $Pe_0 = 10$ ,  $p_s = 1$ ,  $c_c = 9190 \text{ mol/m}^3$ ,  $T_r = T_0 + 300^\circ$  and  $X_f = 15\Phi$ .

**FIGURES:**

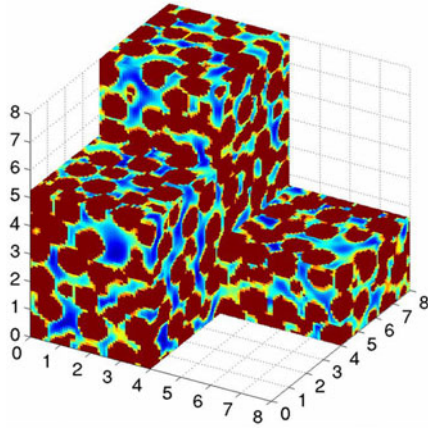


**Figure 1.** Example of a numerically deposited grain packing. Colors in the pore space corresponds to the magnitude of the gas velocity.

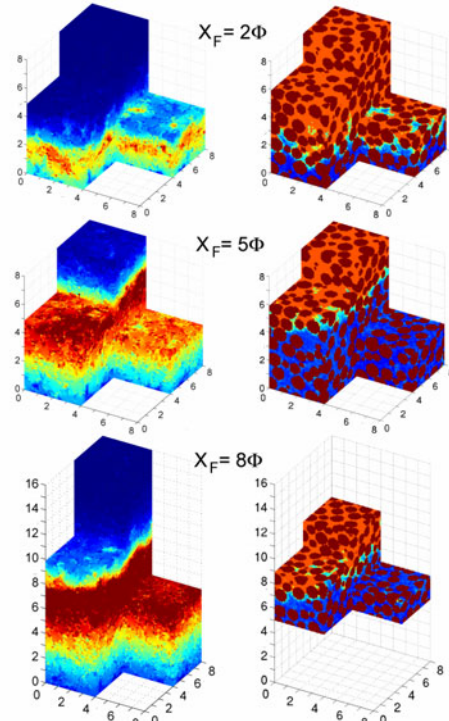


**Figure 3:** Ignition stage in a 3D bed of spheres. The temperature field is shown on the left for three successive positions  $X_f$  of the reaction. The corresponding oxygen concentration fields are shown on the right. Data are for  $Pe = 10$ ,  $p_s = 1/2$ ,  $c_c = 9190 \text{ mol/m}^3$ ,  $\Delta = 0.34$  and  $Pe_{Fs} = 1.45$ .

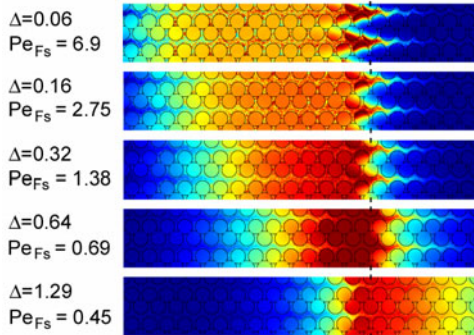


**Figure 2:** Temperature field during a smoldering process in a 2D array of cylinders in various regimes.

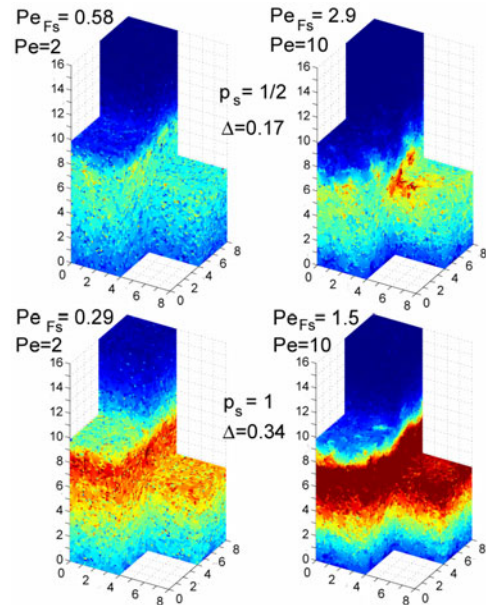


**Figure 4:** The temperature fields in four situations when  $X_f = 8\Phi$ , for  $c_c = 9190 \text{ mol/m}^3$ . The same scale is used in the all cases.

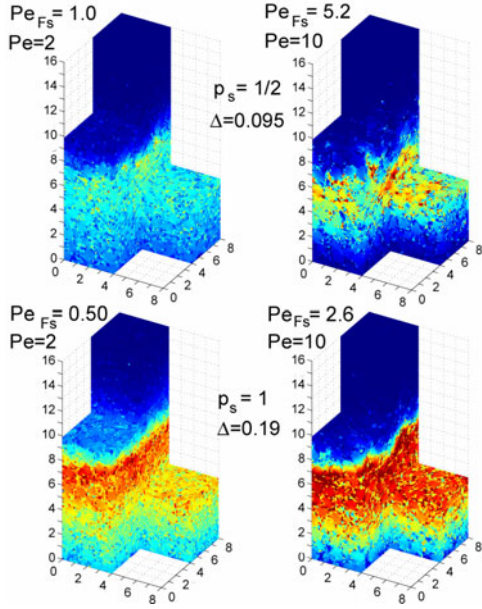


**Figure 5** : The temperature fields in four situations when  $X_F = 8\Phi$ , for  $c_c = 5195 \text{ mol/m}^3$ . The same scale is used in the all cases.

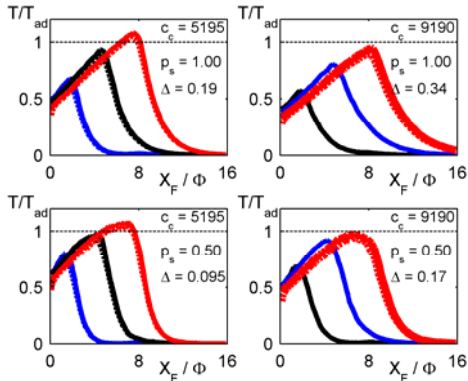


**Figure 6** : Transversally averaged temperature profiles in the four situations in Figs. 4,5 with  $Pe = 2$ , when  $X_F = 2\Phi$ ,  $5\Phi$  and  $8\Phi$ . The dashed line shows the adiabatic temperature  $T_{ad}$  in each situation.

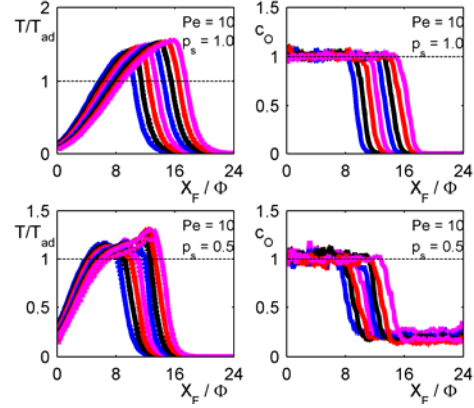


**Figure 7** : Mean profiles of  $T$  (left) and  $c_O$  normalized by the entry gas concentration (right), at successive and regularly spaced instants. Data are for  $Pe = 10$ ,  $p_s = 1$ ,  $c_c = 9190 \text{ mol/m}^3$ ,  $T_r = T_\theta + 300^\circ$  and  $\Pi_r = 1$ .

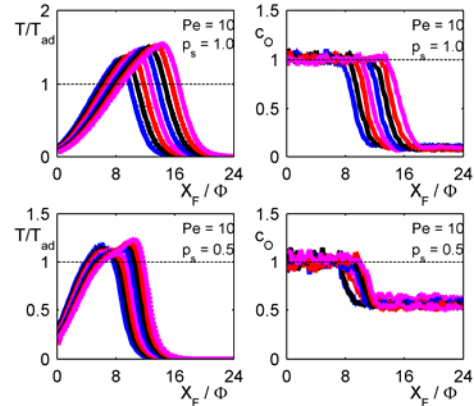


**Figure 8** : Mean profiles of  $T$  (left) and  $c_O$  normalized by the entry gas concentration (right), at successive and regularly spaced instants. Data are for  $Pe = 10$ ,  $p_s = 1$ ,  $c_c = 9190 \text{ mol/m}^3$ ,  $T_r = T_\theta + 300^\circ$  and  $\Pi_r = 0.02$ .

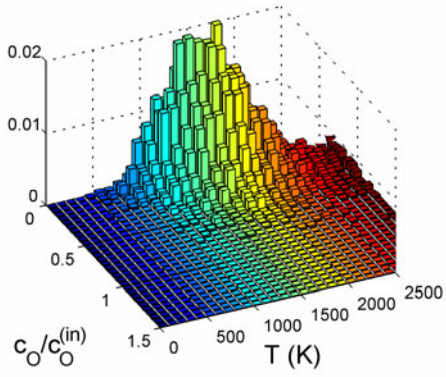


**Figure 9:** Thermochemical conditions at the reaction sites. Data are for  $Pe = 10$ ,  $p_s=1$ ,  $c_c= 9190 \text{ mol/m}^3$ ,  $T_r=T_0+300^\circ$  and  $X_F=15\Phi$ .

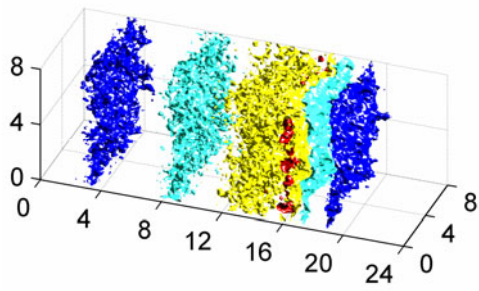


**Figure 10:** Boundaries of the regions where  $T$  exceeds  $T_r = 300^\circ\text{C}$  (blue),  $T_{ad}=1076^\circ\text{C}$  (cyan),  $T_p=1630^\circ\text{C}$  (yellow) and  $2000^\circ\text{C}$  (red). The axes are graduated in grain sizes  $\Phi$ . Data are for  $Pe_O = 10$ ,  $p_s=1$ ,  $c_c= 9190 \text{ mol/m}^3$ ,  $T_r=T_0+300^\circ$  and  $X_F=15\Phi$ .